IAC-19-C4.8-B4.5A.6x52832

Freeform Propellant Delivery System for Cubesats (F-PoDS)

A.V. Steckel[a]*, H. Delecki, W. Ren, K. Thompson

[a] *MIT Lincoln Laboratory, Mechanical Engineering Group*, now available at: amst7410@colorado.edu
* Corresponding Author

Abstract

Additive manufacturing (AM) techniques enable the construction of a freeform fuel storage tank which leverages the underutilized volume in the interior of the cubesat. In the absence of acceleration or gravity, surface tension of the liquid monopropellant can be exploited to control its shape and location within a tank pressurized by an inert gas. This technique requires the use of a propellant management device (PMD) to constrain the fuel to the outlet and reject intrusion of gas bubbles from the pressurizing gas. The interaction between the fuel and PMD is of critical importance to the system design, and a primary factor in this relationship is the liquid adhesion and wetting of the fuel to the PMD surface. This adhesion is a function of both the construction and condition of the materials involved. In this paper we report measurements on the adhesion of deionized water and hydrogen peroxide to AM surfaces. A modified Wilhelmey Plate method is used to measure adhesion tension, and surface tension measurements are done to validate the quality of the experiment. The PMDs tested include a flat coupon to measure contact angle on the AM surface, a simple Jaekle sponge PMD to measure the capillary rise effect, and a lattice inside the sponge PMD. These measurements will be used to assess the impact of AM materials on system performance and deliverable fuel volume.

Keywords: *propellant management device, propulsion, hydrogen peroxide, additive manufacturing, cubesat*

1. Introduction

Cubesats are primarily volume, rather than mass or power, constrained. 1U (10cm x 10cm x 10cm cube) is on the order of the smallest chemical monopropellant systems currently in development [1, 2]. On a 6U cubesat, 1U is 16% of the entire volume budget. To maximize payload capacity, this paper proposes propulsion systems with a flexible form factor to provide the exact amount of thrust necessary for the mission. This is likely to be most useful for missions that require relatively small volumes of propellant, which could fit into existing unusued volume spaces.

To illustrate this, Figure 1 shows the volume allocation for a cubesat modelled after the MS-130 currently under development by Aerojet Rocketdyne [1]. The subsystems are modelled as rectangular blocks with the payload colored cyan, the propulsion colored blue, and the other components grey. The image on the left shows the volume allocation for a 3U cubesat with the 1U propulsion system at the top. The right side image indicates a propulsion system integrated with the spacecraft structure, which is intended to hold only enough fuel to preform necessary operations. Note that this cartoon is not based on requirements for any kind of mission and the same subsystems are present in both. The reduction in fuel volume and flexible form factor increases the space for the payload.

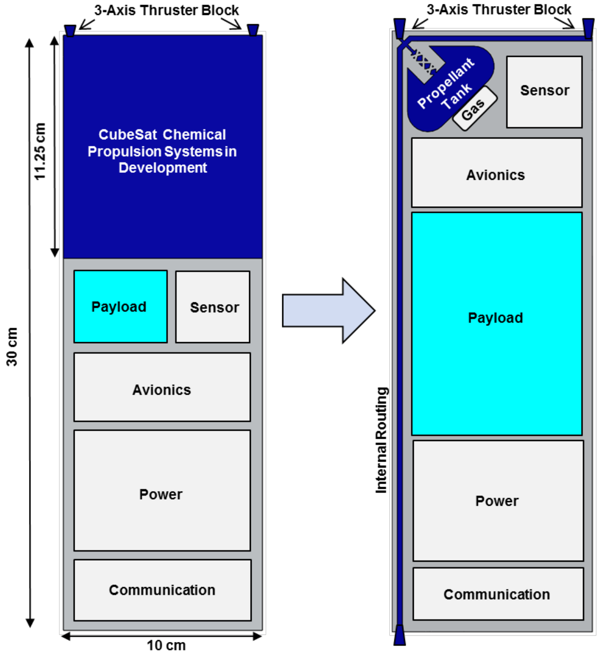

Figure 1: Schematic of sample small sat volume distribution

The key to this technology is the propellant management device (PMD), which controls the location of liquid propellant. In a surface tension tank there is no barrier between the pressurant (gas) and the propellant (liquid), so the PMD ensures the system delivers only liquid fuel (with no gas bubbles) to the catalyst bed. PMDs are simple and require no moving parts, and if required for the mission they can also control the propellant's center of gravity. They have flown on

This material is based upon work supported by the United States Air Force under Air Force Contract No. FA8702-15-D-0001. Any opinions, findings, conclusions or recommendations expressed in this material are those of the author(s) and do not necessarily reflect the views of the United States Air Force.

dozens of spacecraft missions [3], but none for CubeSat fuel tanks at 10cm in diameter or smaller.

This paper will overview the considerations related to the material finish on a PMD surface and overview the constraints enforced by the 3D printing process in section 2. Section 3 will overview the measurements of surface and adhesion tension for both 91% hydrogen peroxide and deionized water and compare them to known values. Section 4 will expand the measurements to estimate the capillary effects of the PMD in deionized water and compare them to theoretical expectation. The concluding section will explore the results and describe future directions.

2. PMD Design Considerations

If AM is used to print a fuel delivery system into a cubesat structure, the internal surfaces will likely have to be left in the 'as printed' condition. This surface roughness is a key design variable for PMDs as it affects the wetting of the propellant to the inner walls. A 3D printed surface has an inherent roughness that changes the contact angle as a function of the surface itself. This effect is shown in **Error! Reference source not found.** and changes the volume of liquid that can be stored in a sponge type PMD, Figure 3. The surface roughness of the internal surface can be modified through a variety chemical polishing techniques, which were not explored here [4].

2.1 *Governing Equation for Sponge PMD*

The approach outlined by Jaekle [5] is used to create an initial PMD design. When the thruster valve opens (during firing), a pressure differential will force the propellant out of the sponge and to the thruster. Figure 2 shows the thruster burn time is restricted to the volume stored in the PMD and the thrust cycle rate is restricted by the PMD fill rate.

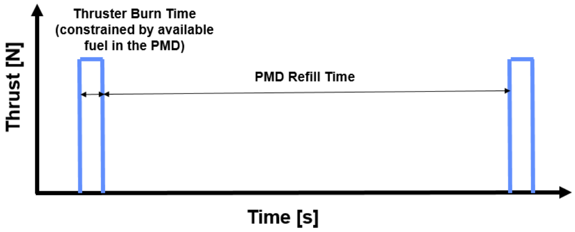

Figure 2: Time for burn vs. PMD refil time

This assumes flow loss from the PMD is negligible, and only applies when the thruster valve is closed. In the hydrostatic case, surface tension is balanced with the acceleration by the Equation 1 and shown in Figure 3 [5].

$$\sigma\left(\frac{1}{R_{up}}-\frac{1}{R_{low}}\right)=\frac{\rho a}{\sin\left(\frac{\pi}{N}\right)}\left(R_{up}+R_{low}\right) \qquad 1$$

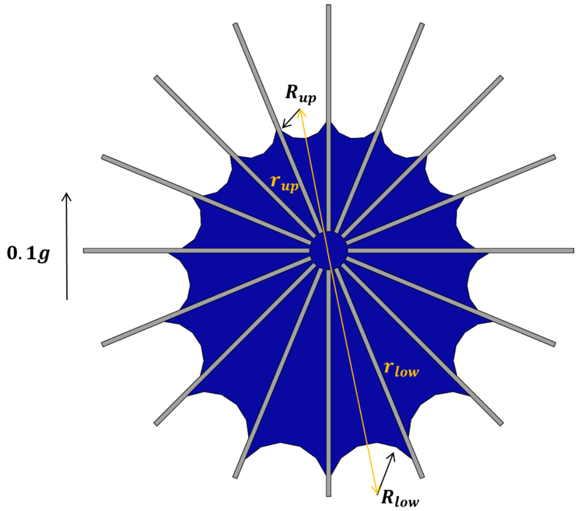

Figure 3: Sponge PMD

Where σ is the liquid surface tension, R_{up} is the smallest liquid radius, R_{down} is the largest liquid radius, ρ is the liquid density, a is the applied acceleration, and N is the number of fins, 24 in this test apparatus. The solution of the governing equation forms the surface of the liquid, Figure 4, and delivers the minimum and maximum fill volumes for a given acceleration. The fill volumes are restricted by the radius of the propellant fluid where excessively large radii will drip out of the sponge. The 3D printed material increases the contact angle of the propellant in the sponge, which results in a smaller volume of propellant contained in the sponge.

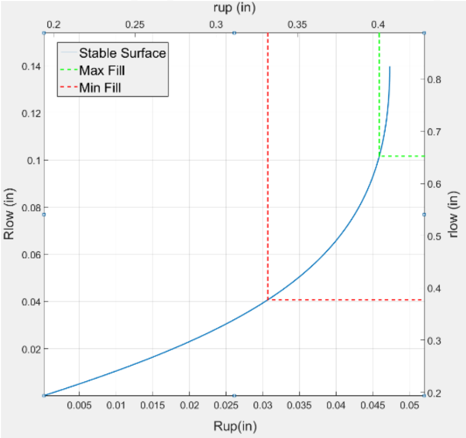

Figure 4: Solution of Liquid Surface

In this model the forces in center of the PMD are neglected and assumed to be full of liquid (this area will be filled by a lattice to enforce this).

2.2 *Contact Angle for 3D Printed Surface*

Increasing the roughness of a surface decreases its contact angle [6, 7]. A large contact angle between the liquid and solid indicates a lower force between the solid and liquid, so the assumption of a 0° contact angle is not conservative. Wenzel's equation, $Cos(\theta_m) = rCos(\theta)$,

This material is based upon work supported by the United States Air Force under Air Force Contract No. FA8702-15-D-0001. Any opinions, findings, conclusions or recommendations expressed in this material are those of the author(s) and do not necessarily reflect the views of the United States Air Force.

relates the ideal contact angle (θ), measured contact angle (θ_m), and surface roughness (r). Young's equation is modified with Wenzel's equation to assess the adhesion force (rA) of the liquid to the surface as a function of the contact angle and surface tension.

$$rA = \sigma_{lg} \cos\theta_m \tag{2}$$

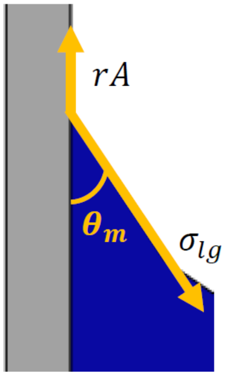

Figure 6: Force Balance of liquid droplet

Each of these three parameters will be independently measured for the 3D printed aluminum surface. The roughness ratio [8] was calculated by the area factor, S_{dr},

$$r = 1 + \frac{S_{dr}}{100} \tag{3}$$

The area factor was measured with a Taylor Hobson CCI white light interferometer and shown in Figure 7. The surface tension is measured from the zero degree initial contact measurement detailed in Section 3 and the adhesion tension is calculated from the submerged coupon measurements, also detailed in Section 3. The AM aluminum material, alloy AlSi10Mg, used in this work has an unknown ideal contact angle. However, for an ideal solid aluminum surface in DI water, the expected Young's contact angle is 72°, however it has been measured to be between 69° and 100° [9, 10, 11, 12], depending on temperature, alloy, and surface treatment.

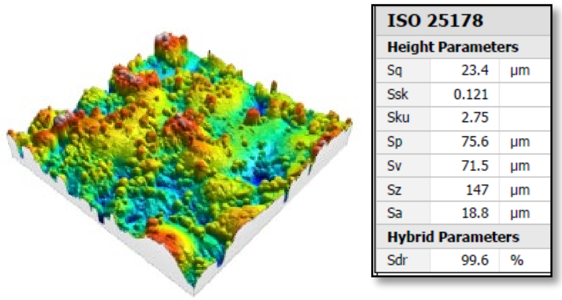

ISO 25178		
Height Parameters		
Sq	23.4	µm
Ssk	0.121	
Sku	2.75	
Sp	75.6	µm
Sv	71.5	µm
Sz	147	µm
Sa	18.8	µm
Hybrid Parameters		
Sdr	99.6	%

Figure 7: Interferometer Measurement

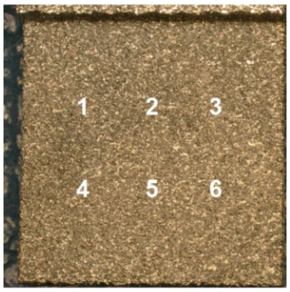

Figure 5: Measurement locations

Test coupons were printed using a DMLS printed with AlSi10Mg powder [13]. Area factor is measured in 6 locations on each side of the tested coupons, as shown in Figure 8. Three different lengths are tested (short, medium, and long). Different orientations and locations on the build plate were tested, but not found to be significant drivers for area factor. The measurements were averaged and the results, including the standard deviation, are summarized in Table 1. Samples were precision cleaned following a standard practice of vapor degrease and ultrasonic IPA bath and kept clean throughout testing. DI water testing was performed first, which includes the samples sitting in DI water overnight. H2O2 testing was done on August 7 2019, when samples sat in 91% concentration H2O2 for ~4 hours. After testing was complete, samples were rinsed with DI water, dried with N2, and roughness was re-measured. In general, Table 1 shows that roughness of the samples increased after contact with H2O2. Compatibility between H2O2 and AlSi10Mg was unknown at the time of testing. During the test there no visible sign of a reaction, however the roughness increased by a statistically significant amount post testing.

Table 1: Coupon Roughness Measurements

Length	Side	Sdr Before H2O2	Sdr After H2O2	% Diff
Short	A	108 ± 15	123 ± 27	14%
Short	B	105 ± 19	119 ± 15	14%
Medium	A	99 ± 17	111 ± 37	12%
Medium	B	105 ± 9	130 ± 16	23%
Long	A	107 ± 23	137 ± 20	29%
Long	B	109 ± 22	145 ± 18	32%

2.3 *Fuel Tank Design*

An integrated fuel tank was printed for testing as shown in Figure 8. The functional components of this system are the pressurant tank, the passive pressure regulating valve, the propellant tank, the PMD, and the propellant outlet. AM enables fabrication of complex

This material is based upon work supported by the United States Air Force under Air Force Contract No. FA8702-15-D-0001. Any opinions, findings, conclusions or recommendations expressed in this material are those of the author(s) and do not necessarily reflect the views of the United States Air Force.

systems that make the propulsion system customizable and modular, as long as the unique fabrication constraints are well understood. This also allows integration of the fuel tank into the spacecraft structure. For a flight system, 316 Stainless Steel is compatible with H2O2. Since the design constraints and roughness are very similar with aluminum 3D printing, in-house capabilities of 3D printing aluminum were leveraged for this research.

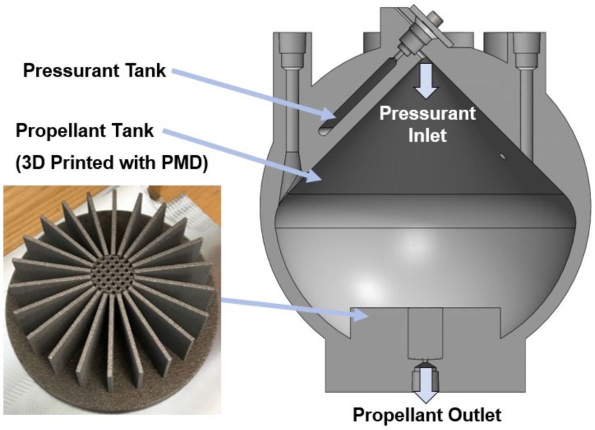

Figure 8: Integrated system

The PMD is based on a previously published design by Jaekle's [5] for direct comparison, with the addition of a lattice in the center tube. Additional mass constraints of 500g were placed on the PMD to allow use with a load cell for measurements that will be discussed in Section 3. The width of the PMD's panels is a balance between printable structure and maintaining the taper required to push gas bubbles away from the center tube and outlet. The final constraint is critical to prevent gas from reaching the outlet. Future flight designs should consider the risk of gas isolating propellant within the PMD and preventing it from reaching the outlet, but this was not a driver for this design, which is used to correlate the experiment to theory.

The tapered walls ensure that the surface tension forces acting from the propellant on the bubble exceed hydrostatic forces pushing the bubble out of the center. This force balance is expressed as:

$$\sigma\left(\frac{1}{R_{in}}-\frac{1}{R_{out}}\right)=\rho a \Delta z \quad 4$$

Where R_{in} is the inner radius, R_{out} is the outer radius, and Δz is the size of the bubble. The minimum required panel taper required for gas rejection can be found by expressing R in terms of panel gap g, and differentiating with respect to z. The resulting minimum taper constraint is:

$$\frac{dg}{dz}>\frac{\rho a g^2}{2\sigma cos(\alpha)} \quad 5$$

The center tube of the PMD is too large to rely on surface tension or capillary action to prevent gas injection due to the 0.04" gap between panels required to remove powder after printing. A porous device is therefore added to block gas bubbles, shown in Figure 9. The bubble point pressure (**ΔP_{BP}**) defines performance of a porous device. This is the minimum pressure required to prevent gas from flowing through the barrier. For this system, the bubble point is 200 Pa, resulting in a maximum pore radius, *r*, of 1mm as derived from Young-Laplace Equation:

$$\Delta P_{BP}=\frac{2\sigma cos(\theta_C)}{r}=200\ Pa \quad 6$$

where θ_C is the pore contact angle between the liquid and screen [14, 15]. With this constraint, a lattice was added to the central tube with MAGICS software and printed to determine if its geometry was printable. 5 different lattice options with the 1mm gap are tested in this paper.

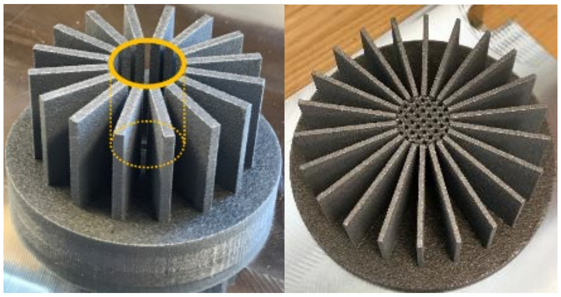

Figure 9: "Center Tube" of PMD and Final PMD with Lattice

A Matlab routine was developed to select an optimal PMD design over the indicated panel thicknesses and number of panels, Figure 10. The minimal panel thicknesses was determined based on in house testing and approximating the fin as a cantilevered beam. This could possibly be reduced with further printer development. The color bar indicates the volume in the PMD and reveals a reduced trade space of available designs to select from when considering manufacturability and effectiveness.

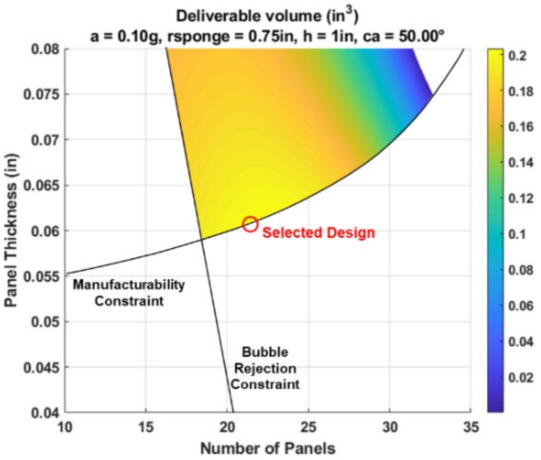

Figure 10: PMD Deliverable Volume Trade

This material is based upon work supported by the United States Air Force under Air Force Contract No. FA8702-15-D-0001. Any opinions, findings, conclusions or recommendations expressed in this material are those of the author(s) and do not necessarily reflect the views of the United States Air Force.

The final design of the PMD is:

- Minimum sponge radius 1”
- 22 panels, .06” thick
- 1” tall
- Center tube filled with lattice with a maximum 1 mm radius hole
- Deliverable fuel volume: 0.21 in^2
- Limiting acceleration for gas rejection: .12g
- Bubble Point: 200 Pa

3. Measurement of Adhesion and Surface Tension

The Wilhelmy Plate method [16, 17] is selected to measure the surface tension, adhesion tension, and contact angle. Although more accurate alternative techniques are available [10], this method was selected to enable low-cost assessment of the performance of the PMD without requiring a 0g test. This initial step may provide a useful quality check for future and more complex systems.

The apparatus is shown in Figure 11. To measure the PMD properties, a load cell is raised and lowered with a lab jack. The load data were collected at a frequency of 8000 Hz on a National Instruments data acquisition system. The height of the lab jack was monitored with a calibrated dial gauge and the H2O2 and DI water were kept in clean glassware. A vibration isolating table was used to prevent room noise (~5-10 mN) from affecting the data.

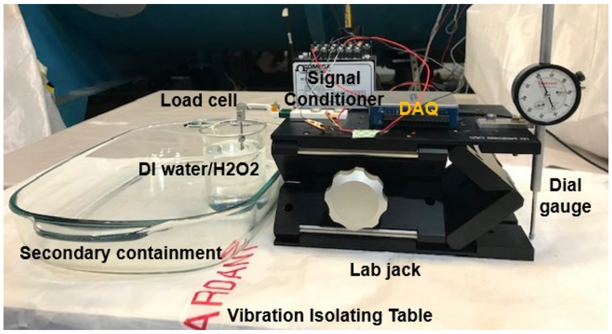

Figure 11: Wilhelmy Plate Experiment Setup

The experimental procedure compromised of raising and lowering various samples into the liquid. As the samples were drawn into and out of a liquid bath, the force on the load cell was monitored in real time. Figure 12 shows the vector forces from the water surface measured while the coupon is submerged and correlate with Equation 2. There are additional forces acting on the system from the bulk liquid, such as buoyancy, which IS observed and accounted for.

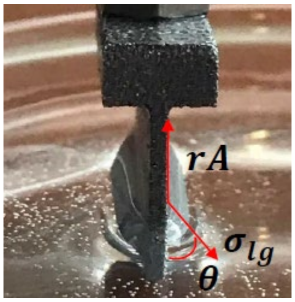

Figure 12: Submerged Coupon

Figure 13 shows a typical output from the DAQ for a single measurement with a coupon inserted and removed from the liquid bath. A matlab script was developed to highlight and calculate the pertinent features of each data set. The black data are the baseline force of the coupon on the strain gauge, not touching the water. As the coupon is lowered into the fluid, the initial large feature in the force plot is from the surface tension of the first interaction between the water and the coupon. This force occurs when the contact angle is zero and the surface tension can be directly measured and compared with published values [18, 19]. After breaking the surface of the liquid, the coupon becomes fully submerged and the liquid is allowed to find the steady state solution, shown in Figure 12, defined by the lowest energy of the liquid and metal surface interaction. The red data in Figure 13 show this force measured on the strain gauge when the liquid is adhered to the surface. Utilizing Equation 2 and the difference between the adhered forces, dry forces, and surface tension, the contact angle can be calculated.

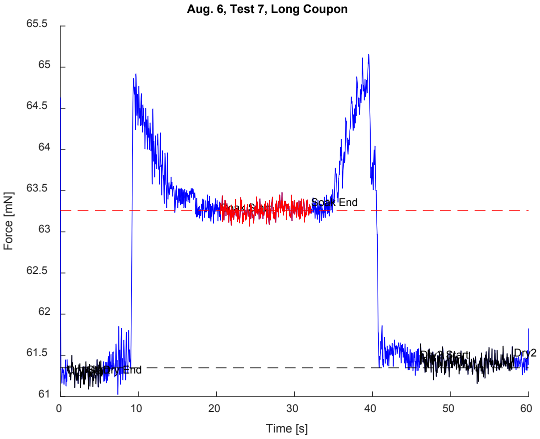

Figure 13: Measured Coupon Force

3.1 Measurements on Test Coupons

This process is conducted for several different coupons and many different penetration depths. By using different coupon geometries and submersion depths, the variations due to surface inconsistencies, buoyancy, and material geometry will be averaged. Table 2 compiles data from several runs for surface and adhesion tension

This material is based upon work supported by the United States Air Force under Air Force Contract No. FA8702-15-D-0001. Any opinions, findings, conclusions or recommendations expressed in this material are those of the author(s) and do not necessarily reflect the views of the United States Air Force.

and the percent difference between the published surface tension and the one measured in this apparatus.

Table 2: Adhesion and Surface Tension Results

Coupon Description	Adhesion Tension (mN/m)	Surface Tension (mN/m)
H_2O Small	62.7 ± 1.3	89.4 ± 3.7
H_2O Long	58.6 ± 4.5	72.6 ± 1.1
H_2O_2 Small	60.7 ± 0.7	80.6 ± 2.6
H_2O_2 Medium	58.4 ± 1.1	77.2 ± 3.3
H_2O_2 Long	58.4 ± 0.8	73.7 ± 1.9

This data shows that for 3D printed aluminum surfaces where adhesion and surface tension are the primary forces, deionized water and hydrogen peroxide behave in similar ways. There are larger variations in the measurements of surface tension than adhesion, this is attributed to the mounting method used in the test. A skewed coupon will contact the surface with slightly different cross section will adhere to the surface at first contact. This will affect the force peak shown in Figure 13. For adhesion, the entire cross section is submerged and at equilibrium and therefore will be wet.

The measured contact angle, θ_m, of H2O2 and H2O can be computed for these rough 3D printed surfaces utilizing Equation 2 and the measurements summarized in Table 1 and Table 2 to be, 41.5 ± 8.2 for DI water and 40.0 ± 3.8 H2O2. Using Wenzel's equation and the measured surface roughness, the ideal Young's angle, θ, for the Al liquid interface can be calculated. The value for DI water is 69.8 ± 3.6 and for H2O2 is 69.3 ± 2.8. The contact angles for the individual coupons are summarized in Table 3.

Table 3: Coupon Contact Angles

Coupon Description	Contact Angle
DI Water Small (measured)	29.2 ± 2.1
DI Water Long (measured)	35.4 ± 5.8
DI Water (Young's)	69.8 ± 3.6
H_2O_2 Small (measured)	32.5 ± 1.0
H_2O_2 Medium (measured)	36.4 ± 0.5
H_2O_2 Long (measured)	35.8 ± 1.1
H_2O_2 (Young's)	69.3 ± 2.8

3.2 *Measurements on PMD*

Utilizing this same apparatus, the performance of the PMD can also be assessed. The mass of the liquid adhered to the PMD is measured. The value can be broken into two components: the first is the volume held by the adhesion to the sponge fins (same as the coupons) and the second component is due to the geometric effects of capillary rise between two angled parallel plates [20, 21]. The average adhesion per unit length across all coupons for a given liquid is used to estimate the volume adhered to the surface of the PMD, the "fin adhesion". The difference between the measured liquid mass and the fin adhesion is therefore estimated to be the mass of liquid captured by capillary rise. For a PMD with no internal sponge, the adhesion force of DI water is 42.9 ± 0.1 mN. The fin adhesion is 36.9 ± 2.4. The measured force of the capillary water is therefore 12.3 ± 2.4.

This volume is approximately calculated by modifying the capillarity pressure for a circular capillary and equating the radial height profile to a distance from the PMD plate surface. The capillary pressure is calculated following the approach in Rapp [22] where H is the liquid height along the symmetry lines between the fins, x is the radial distance, α is the angle between fins, and d is the plate separation

$$H = \frac{4\,Cos(\theta) * \sigma}{r * \rho g} \qquad \mathbf{7}$$

This capillary rise has two components, the height, detailed in Equation 7, and the meniscus on top of the fluid. It is assumed that the meniscus contribution is accounted for by the already calculated adhesion force. The total capillary rise force and volume is calculated by the volume integral bound in the z axis by the capillary height, the theta direction by the plate walls, and in the radial direction by the minimum plate separation on the inner radius and on the outer radius by the capillary length. The capillarity length [22] is defined as,

$$L_c = \sqrt{\frac{\sigma}{\rho g}}$$

Completing this exercise, we arrive at a capillary rise force of 7.1 ± 1.2 mN.

3.3 *Measurements on PMD with Lattice*

Utilizing this same apparatus, the performance of the PMD with the center lattice (shown in Figure 9) can also be assessed. In this case, the adhesion tension can be broken into 3 volumes: fin adhesion (from section 3.2), liquid wicking into the sponge from the capillary rise effect (from section 3.2), and liquid inside the lattice in the center tube. MAGICS software was used to generate 5 different lattice options which all met the maximum pore diameter criteria from eq. 6. Each were 3D printed for testing, shown in Figure 15.

The buoyancy affecting the PMD is different depending on the geometry of the lattice, and was included. The theoretical capillary rise for this PMD was estimated by first computing the theoretical value, 9.4 ± 1.7 mN, following the same approach described in section 3.2. This was scaled by the ration of the measured value to the predicted value of the PMD with no lattice (12.3/7.1) to an estimated capillary rise force of 16.4 ± 3.2 mN. The force of liquid in the lattice equals Total PMD Adhesion – Capillary Rise – Fin Adhesion. Table 4

DISTRIBUTION STATEMENT A. Approved for public release. Distribution is unlimited.

This material is based upon work supported by the United States Air Force under Air Force Contract No. FA8702-15-D-0001. Any opinions, findings, conclusions or recommendations expressed in this material are those of the author(s) and do not necessarily reflect the views of the United States Air Force.

shows the different adhesion results for the different lattice shapes. Note that the experiment was run at depths of 0.1” and 0.15”. The volume of liquid in the lattice was observed to be smaller by the percent listed in Table 4 for all lattices. The physical explanation for why this would be is not well understood, and requires further investigation. Many of these differences are within the error of the experiment. Lattice 2 is in the top right corner of Figure 15, and is the only lattice that has the pores open all the way through to the outlet (shown in Figure 15). It is not surprising that this resulted in poorer liquid adhesion, but this is the only geometry that lets the ends of the lattice meet, providing greater structural strength.

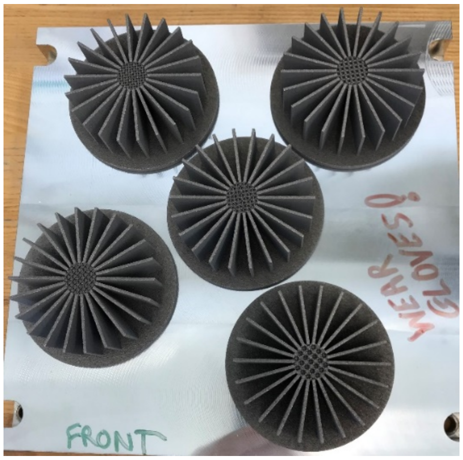

Figure 14: PMDs with Lattices on Build Plate

Table 4: Lattice Adhesion Results

Lattice ID	Total PMD Adhesion (mN)	Lattice Liquid Volume (mL)	% Decrease in Volume at Depth 2
Lattice 1	115.7 +/- 1.6	6.4 +/- 0.4	2.6%
Lattice 2	98.2 +/- 0.5	4.6 +/- 0.4	13.7%
Lattice 3	108.6 +/- 0.2	5.7 +/- 0.4	3.3%
Lattice 4	112.9 +/- 0.01	6.1 +/- 0.4	2.0%
Lattice 5	113.6 +/- 0.7	6.2 +/- 0.4	2.2%

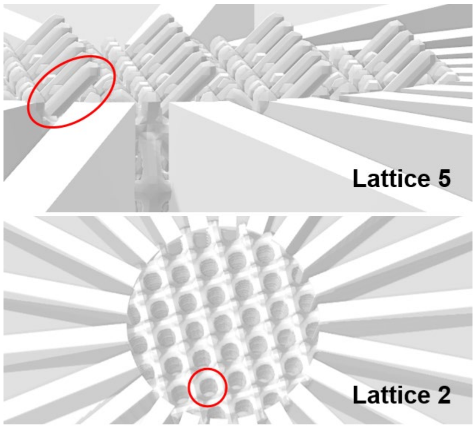

Figure 15: Lattice Geometry Detail

6. Conclusions

For the complex geometries of additively manufactured fuel storage and feed systems, the Wilhelmy Plate method is used to characterize the trapped volume of fuel in a PMD under normal gravitational conditions. The trapped volume is further broken down into the liquid stored in the fins and the liquid stored in the central lattice of the PMD. This method demonstrates a path forward for an experimental tool to characterize PMD performance without zero gravity measurements. In addition, the contact angle, adhesion tension, and surface tension for as-printed, AlSi10Mg is measured for both deionized water and 91% hydrogen peroxide are measured and compared to published values for similar material. These results show a probable path forward for future integrated, 3D printed, and flexible fuel storage and feed systems for cubesats

Acknowledgements

Support and collaboration from the MIT LL engineering division was critical for the success of this research initiative. Many students, co-ops and summer interns also contributed to the work. This includes Bob Davis, Mark Padula, Sean Crowley, Steve Gillmer, Kyle Thompson, Adam Shabshalowitz, Jesse Mills, Ryan Flanigan, Tom Sebastian, Harrison Delecki, Jesus Aponte, Brandon Henley, and Finn O’Brien.

Appendix A (Aspect Ratio of PMD)

The optimal orientation to print the PMD is vertical due to the shape of the panels and lattice. Printing thin vertical walls introduced manufacturing challenges. The manufacturability constraints were determined expirementally. Representative PMD panel walls of various hieght to thickness ratios were printed and inspected for damage. Orientation with respect to the cutting blade and aspect ratio were the two critera that drove the success of the print.

This material is based upon work supported by the United States Air Force under Air Force Contract No. FA8702-15-D-0001. Any opinions, findings, conclusions or recommendations expressed in this material are those of the author(s) and do not necessarily reflect the views of the United States Air Force.

Orientation of the PMD with respect to the cutting blade is critical to manage during printing. It is important to avoid a 90° angle with cutting blade.

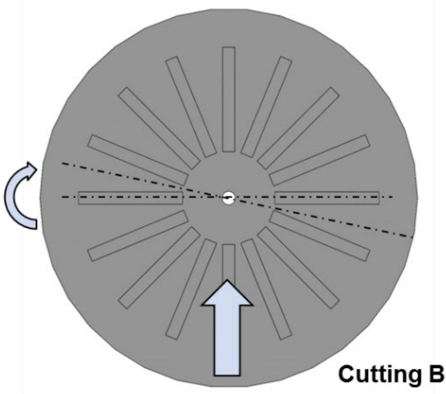

The fin aspect ratio (AR) is critical to get a successful print. We iterated on this once by printing in house and saw failures with an aspect ratio of 12.5. With a slight reduction in aspect ratio (11.25), the print was successful.

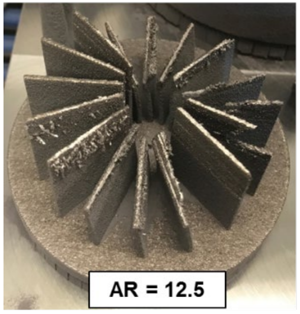

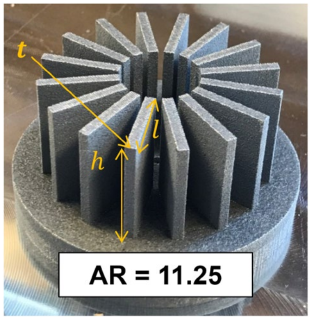

Alternate criteria was considered to evaluate manufacturability based on bending stress of a thin plate. This was used in the matlab trade illustrated in Figure 10.

$$\sigma_{max} = \frac{6M}{It^2}$$

First print (failure):	$\frac{\sigma_{max}}{F_{blade}} = 3000\ in^{-2}$
Second print (success):	$\frac{\sigma_{max}}{F_{blade}} = 1205\ in^{-2}$

Appendix B (Integrated Tank Fabrication)

In order to remove powder after printing, each cavity must have at least 2 openings- one to insert gas to blow the powder out, and 1 exit for the powder. The flow chart shown below depicts the step by step process required to ensure that all debris is removed from the interior volume and ensure that the cavities are sealed.

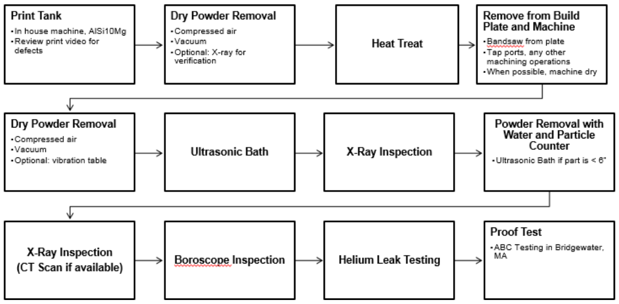

Tank validation flow chart

Once the tank is printed, a gross cleaning occurs with pressurized gas and a vacuum. To ensure that the majority of the material has been removed various imaging techniques can be used. With the gross powder removed, the sintered material is heat treated to further solidify the walls. The part is removed from the build plate and cleaned once again with dry gas and a vacuum, before more powder is sonically dislodged. The final five stages of the flow chart verify that the tank produced is as designed.

A “scoop” design has been incorporated to improve the flow of powder out of the chamber. These scoops required a detailed finite element analysis of the tank to consider high stress concentrations at these locations in the tank. In house processes were leveraged for additional powder removal. DI water was circulated through the tank to remove traces of powder. A particle counter measured particulate levels, and a filter removed particles as water circulated. This has the additional benefit of verifying the system won’t clog. The table below summarizes particle counts measured during this process, and in the final state.

Particle Levels during DI Cleaning

Particle Size (um)	Particle Count at Start (/ml)	Particle Count at End (/ml)
> 25	>100	0
15-25	>100	<3
10-15	>1000	<10
5-10	>3000	<50

Some anomalies during print were identified during a boroscope inspection of the channels. A void which looks like a possible crack initiation site is photographed. This was located on the internal wall of the channel, and was not a threat to the outer walls of the tank. However, the boroscope is limited in with a short view distance, which means only the narrow channels and interfaces to the larger tanks can be inspected. This means there could be other voids printed in the larger chambers, where we cannot inspect. Funding for a CT scan (which has enough resolution to image these kinds of voids) was not originally budgeted, and was found to be prohibitively expensive. The tank was imaged with the in house X-ray,

This material is based upon work supported by the United States Air Force under Air Force Contract No. FA8702-15-D-0001. Any opinions, findings, conclusions or recommendations expressed in this material are those of the author(s) and do not necessarily reflect the views of the United States Air Force.

and the build video was reviewed to attempt to identify other locations with anomalies. The anomaly was identified in the build video, as shown below.

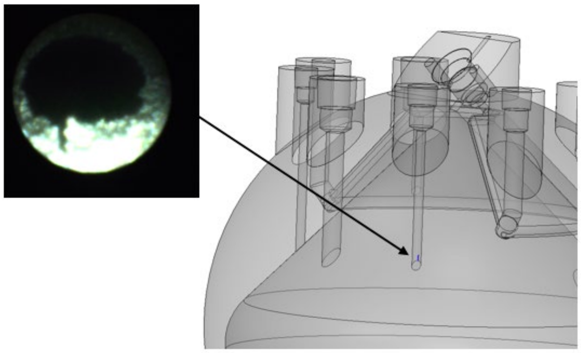

Figure 16: Print Anomaly

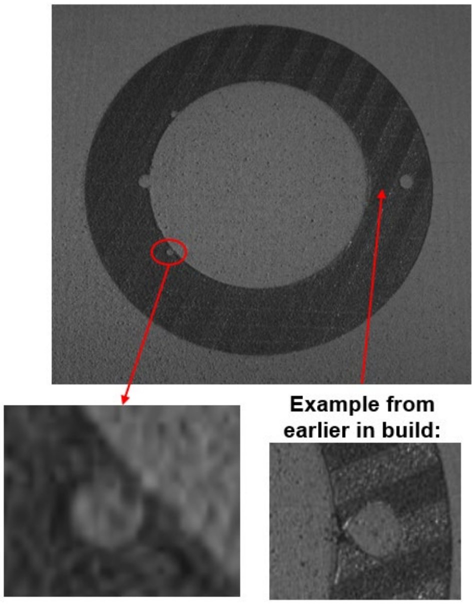

Images of Print Anomaly in Build Video

The completed tank was checked for leaks with a standard helium 4 mass spectrometer. The leak rate from propellant tank and pressurant tank to atmosphere, as well as to one another were shown to have leak rates less than $5x10^{-7}\ mbar\ L/s$. A further test was done where the entire chamber was encased to determine if hairline cracks were present from the 3D printing process.

The tank was proof tested at ABS testing in Bridgewater, MA. This was a hydrostatic test using water as the pressurant, because any failure would be safer than failing with gas pressurant. The tanks were tested to 1.3x Max Burst Disc Pressure. This is more than 2x operating pressure.

Results of the proof test were successful to levels of 340 psi on the propellant chamber and 540 psi on the pressurant chamber. A post-test x-ray showed no deformation.

This material is based upon work supported by the United States Air Force under Air Force Contract No. FA8702-15-D-0001. Any opinions, findings, conclusions or recommendations expressed in this material are those of the author(s) and do not necessarily reflect the views of the United States Air Force.

1. REFERENCES

[1] Aerojet Rocketdyne, "Modular Propulsion System," [Online]. Available: https://www.rocket.com/sites/default/files/documents/CubeSat%20Mod%20Prop-2sided.pdf. [Accessed 01 September 2019].

[2] VACCO Industries, "Cubesat propulsion systems," [Online]. Available: https://www.cubesat-propulsion.com/vacco-systems/. [Accessed 01 09 2019].

[3] J. W. Hartwig, "A detailed historical review of propellant management devices for low gravity propellant acquisition," in *52nd AIAA/SAE/ASEE Joint Propulsion Conference*, 2016.

[4] A. Townsend, N. Senin, L. Blunt, R. K. Leach and J. S. Taylor, "Surface texture metrology for metal additive manufacturing: a review," *Precision Engineering,* vol. 46, pp. 34-47, 2016.

[5] J. D. Jaekle, "Propellant management device conceptual design and analysis-Vanes," in *27th Joint Propulsion Conference*, 1991.

[6] R. Wenzel, "Resistance of Solid Surfaces to Wetting by Water," *Industrial and Engineering Chemistry, vol. 28,* 1936.

[7] A. B. Cassie, "Contact angles," *Discussions of the Faraday society 3,* pp. 11-16, 1948.

[8] R. Deltombe, K. J. Kubiak and M. Bigerelle, "How to select the most relevant 3D roughness parameters of a surface," *Scanning: The Journal of Scanning Microscopies,* vol. 36, no. 1, pp. 150-160, 2014.

[9] A. Faghri and Y. Zhang, Transport phenomena in multiphase systems, Elsevier, 2006.

[10] Z. Q. Zhu, Y. Wang, Q. S. Liu and J. C. Xie, "Influence of Bond Number on Behaviors of Liquid Drops Deposited onto Solid Substrates," *Microgravity Sci. Technol.,* vol. 24, pp. 181-188, 2012.

[11] L. Torrisi and C. Scolaro, "Treatment Techniques on Aluminum to Modify the Surface Wetting Properties," *ACTA PHYSICA POLONICA A ,* vol. 128, no. 1, pp. 48-53, 2015.

[12] B. Taft, S. Smith and J. Moulton, "Contact angle measurements for advanced thermal management technologies," *Frontiers in Heat and Mass Transfer (FHMT),* vol. 5, no. 1, 2014.

[13] T. Lore, K. Kempen, J. P. Kruth and J. Humbeek, "Fine-structured aluminium products with controllable texture by selective laser melting of pre-alloyed AlSi10Mg powder," *Acta Materialia,* vol. 1, no. 61, pp. 1809-1819, 2013.

[14] J. Hartwig and J. McQuillen, "Performance gains of propellant management devices for liquid hydrogen depots," in *51st AIAA Aerospace Sciences Meeting including the New Horizons Forum and Aerospace Exposition*, 2013.

[15] J. W. Hartwig, Liquid acquisition devices for advanced in-space cryogenic propulsion systems, Academic Press, 2015.

[16] E. Rame, "The interpretation of dynamic contact angles measured by the Wilhelmy plate method," *Journal of colloid and interface science,* vol. 185, no. 1, pp. 245-251, 1997.

[17] J. W. Bush, "MIT open courseware: Interfacial Phenomena," 2010. [Online]. Available: https://ocw.mit.edu/courses/mathematics/18-357-interfacial-phenomena-fall-2010/.

[18] M. K. Phibbs and P. A. Giguere, "Hydrogen peroxide and its analogues: 1," *Canadian journal of Chemistry,* vol. 29, no. 2, pp. 173-181, 1951.

[19] A. W. Adamson and A. P. Gast, Physical chemistry of surfaces. Vol. 15, New York: Interscience, 1967.

[20] F. J. Higuera, A. Medina and A. Linan, "Capillary rise of a liquid between two vertical plates making a small angle," *Physics of Fluids,* vol. 20, no. 10, p. 102, 2008.

[21] M. M. Weislogel and S. Lichter, "Capillary flow in an interior corner," *Journal of Fluid Mechanics,* vol. 373, pp. 349-378, 1998.

[22] B. E. Rapp, Microfluidics: Modeling, Mechanics and Mathematics, Elsevier, 2017.

[23] J. R. Wertz and W. J. Larson, "Space Mission Analysis and Design," Third ed., Hawthorne, CA and New York, NY, Microcosm Press and Springer, 1999, pp. 708-716.

This material is based upon work supported by the United States Air Force under Air Force Contract No. FA8702-15-D-0001. Any opinions, findings, conclusions or recommendations expressed in this material are those of the author(s) and do not necessarily reflect the views of the United States Air Force.

[24] R. N. Wenzel, "Resistance of solid surfaces to wetting by water," *Industrial & Engineering Chemistry,* vol. 28, no. 8, pp. 988-994, 1936.

[25] S. W. Smith, The scientist and engineer's guide to digital signal processing, dspguide.com, 1997.

[26] W. C. Schumb, C. N. Satterfield and R. L. Wentworth, Hydrogen peroxide, Reinhold Publishing Corporation, 1955.

[27] D. Schmuland, C. Carpenter, R. Masse and J. Overly, "New Insights Into Additive Manufacturing Processes: Enabling Low-Cost, High-Impulse Propulsion Systems," in *Small Satellite Conference*, 2013.

[28] E. Kulu, "World's Largest Database of Nanosatellites, over 2000 Nanosats and CubeSats," 2018. [Online]. Available: www.nanosats.eu/index.html#figures. .

[29] J. W. Hartwig, Liquid Acquisition Devices for Advanced In-Space Cryogenic Propulsion Systems, Academic Press, 2016.

[30] A. a. Y. Z. Faghri, Transport Phenomena in Multiphase Systems, Elsevier Academic Press, 2010.

[31] A. Faghri and Y. Zhang, Transport phenomena in multiphase systems, Elsevier, 2006.

[32] S. Ebnesajjad, "Surface Energy of Solids," in *Surface Treatment of Materials for Adhesion Bonding*, William Andrew, 2006, pp. 29-42.

[33] J. D.E. Jaekle, "Propellant Management Device Conceptual Design and Analysis: Sponges," *AIAA 29th Joint Propulsion Conference and Exhibit,* 1993.

[34] J. Bush, *18.357 Interfacial Phenomena,* Massachusetts Institute of Technology: MIT OpenCourseWare, https://ocw.mit.edu. License: Creative Commons BY-NC-SA, Fall 2010, p. 9.

[35] J. W. Bush, "Interfacial Phenomena," MIT Open Courseware 18.357, Cambridge.

[36] I. Ballinger, W. Lay and W. J. Tam, "Review and history of PSI elastomeric diaphragm tanks," in *1st Joint Propulsion Conference and Exhibit*, 1995.

[37] "Young's Equation," 9 June 2017. [Online]. Available: www.kruss.de/services/education-theory/glossary/youngs-equation/.

[38] Biolin Scientific, "Technology Note 7," [Online]. Available: https://cdn2.hubspot.net/hubfs/516902/Pdf/Attension/Tech%20Notes/AT-TN-07-Surface-roughness-CA-wettability.pdf. [Accessed 2019].

[39] Attension, "Influence of Surface Roughness on Contact Angle and Wettability," [Online]. Available: http://www.dynetesting.com/.

[40] Ariane Group, "Hydrazine Propellant Tanks Overview," [Online]. Available: http://www.space-propulsion.com/spacecraft-propulsion/hydrazine-tanks/hydrazine-tank-overview.html. [Accessed September 2019].

This material is based upon work supported by the United States Air Force under Air Force Contract No. FA8702-15-D-0001. Any opinions, findings, conclusions or recommendations expressed in this material are those of the author(s) and do not necessarily reflect the views of the United States Air Force.